

# Wafer-Scale and Topologically Nontrivial $\alpha$ -Sn Films Grown on InSb (001) by Molecular-Beam Epitaxy

Yuanfeng Ding<sup>1</sup>, Huanhuan Song,<sup>1</sup> Junwei Huang<sup>1</sup>, Jinshan Yao<sup>1</sup>, Yu Gu,<sup>1</sup> Lian Wei,<sup>1</sup>  
Y. B. Chen,<sup>2,\*</sup> Yu Deng,<sup>1</sup> Hongtao Yuan<sup>1,3,4</sup>, Hong Lu<sup>1,3,4,†</sup> and Yan-Feng Chen<sup>1</sup>

<sup>1</sup>*National Laboratory of Solid State Microstructures & Department of Materials Science and Engineering, College of Engineering and Applied Sciences, Nanjing University, Nanjing 210093, China*

<sup>2</sup>*Department of Physics, Nanjing University, Nanjing 210093, China*

<sup>3</sup>*Jiangsu Key Laboratory of Artificial Functional Materials, Nanjing University, Nanjing 210093, China*

<sup>4</sup>*Collaborative Innovation Center of Advanced Microstructures, Nanjing University, Nanjing 210093, China*

(Received 23 June 2021; revised 9 December 2021; accepted 14 December 2021; published 12 January 2022)

Single-crystalline  $\alpha$ -Sn films on the wafer scale are epitaxially grown on InSb (001) substrates by molecular-beam epitaxy. The Berry phase for  $\alpha$ -Sn is extracted to be  $-0.64\pi$  from the quantum oscillations of the magnetoconductivity. Angle- and temperature-dependent Shubnikov–de Haas oscillations substantiate that the  $\alpha$ -Sn film has a spherical Fermi surface and small effective mass ( $0.039m_0$ ;  $m_0$  is the resting mass of an electron), which are in agreement with the features of three-dimensional Dirac semimetals. In addition, an extremely large magnetoresistance of over  $4.5 \times 10^5\%$  at 1.5 K is observed. These  $\alpha$ -Sn films, with wafer-scale dimensions and extremely large magnetoresistance, may pave the way for device applications of topological materials.

DOI: [10.1103/PhysRevApplied.17.014015](https://doi.org/10.1103/PhysRevApplied.17.014015)

## I. INTRODUCTION

Topological materials represent an emerging quantum state of matter and are intriguing for their topologically nontrivial electronic structures [1–3]. Transport phenomena are extensively investigated to demonstrate these unusual electronic properties in topological materials, such as large magnetoresistance (MR) [4–8], chiral-anomaly-induced negative MR [9], planar Hall effect (PHE) [10–13], weak antilocalization (WAL) [14,15], and spin-momentum locking [16,17]. Among them, Shubnikov–de Haas (SdH) oscillations of MR can reveal the  $\pi$ -Berry phase of Dirac fermions, which is the fingerprint of topological materials [18]. In addition to the physical significance, the magnetotransport properties make topological materials promising for electronic device applications.

$\alpha$ -Sn, also known as gray tin, is an allotrope of tin with a diamond crystal structure. Farrow *et al.* demonstrated epitaxial  $\alpha$ -Sn films using molecular-beam epitaxy (MBE) in 1981 and the alpha phase could be stabilized by the substrate up to room temperature [19].  $\alpha$ -Sn is theoretically predicted to be a zero-gap semiconductor [20], but it is also predicted to change into a topological insulator with biaxial tensile strain and a Dirac semimetal with compressive strain [21–23]. Different from other compound topological materials,  $\alpha$ -Sn is an elemental

material and easy to grow without worrying about non-stoichiometric defects. Stimulated by these advantages, the topological surface states of  $\alpha$ -Sn films are observed by angle-resolved photoemission spectroscopy (ARPES) [24–28]. Transport studies are also reported for  $\alpha$ -Sn [29,30] and even stanene [31,32]. However, direct transport evidence, i.e., a nontrivial Berry phase in  $\alpha$ -Sn, is somewhat difficult to obtain due to the contribution from the conductive substrate. The reported SdH oscillations are still not strong enough, which may be limited by the film quality. More importantly, while most studies focus on the topological insulator phase in  $\alpha$ -Sn, the Dirac semimetal phase in  $\alpha$ -Sn has not been confirmed by transport yet. From the viewpoint of device applications, Dirac semimetal  $\alpha$ -Sn can also demonstrate high spin-to-charge conversion [33] and magnetization-switching [34] efficiencies, as well as the topological insulator phase [35], showing potential for application in spintronic devices. On the other hand, potential magnetotransport properties, such as large or negative magnetoresistance [22], have never been reported experimentally. Based on the abovementioned facts, further exploration of  $\alpha$ -Sn films is valuable.

Here, we successfully grow a series of single-crystalline wafer-scale  $\alpha$ -Sn films on InSb (001) substrates by MBE and observe strong SdH quantum oscillations in a magnetotransport study. Analysis of the SdH oscillations proves that the  $\alpha$ -Sn films have a finite Berry phase and spherical Fermi surface, which are the fingerprints of three-dimensional (3D) Dirac semimetals. In addition,

\*ybchen@nju.edu.cn

†hlu@nju.edu.cn

we observe an extremely large magnetoresistance of over  $4.5 \times 10^5\%$  at 1.5 K and over  $3.0 \times 10^4\%$  within a wide temperature range (100–200 K). These superior physical properties make these wafer-scale  $\alpha$ -Sn films a promising material platform for device applications.

## II. EXPERIMENT

The  $\alpha$ -Sn samples are grown using two MBE systems, a III–V MBE system (Veeco GENxplor) equipped with In (99.999 99%) and Sb (99.999 995%) solid-state sources for InSb treatment and a group-IV MBE system (Dr. Eberl MBE-Komponenten Octoplus 300) equipped with a high-purity Sn (99.9999%) solid-state source for  $\alpha$ -Sn growth. InSb (001) ( $a = 6.480$  Å) substrates are treated in the III–V system to remove surface oxides under a Sb atmosphere, after which an InSb buffer layer is grown to improve the surface quality. The streaky ( $2 \times 4$ ) surface reconstruction is observed by reflection high-energy electron diffraction (RHEED) (see Fig. S1 within the Supplemental Material [36]), indicating a cleaned Sb-stabilized InSb surface. To avoid reoxidation during transfer, an amorphous Sb capping layer is deposited on the InSb surface. Afterwards, the substrate is transferred to the group-IV system, and the Sb capping layer is desorbed thermally before  $\alpha$ -Sn growth. Before  $\alpha$ -Sn growth, the substrate temperature is quickly cooled to well-below room temperature by directly contacting the sample holder with a cooling plate (kept below  $-100$  °C) for 15 min.  $\alpha$ -Sn growth is performed with a background pressure of  $<5 \times 10^{-10}$  mbar. The growth rate is about approximately 0.1 Å/s (approximately 4 monolayers/min). The surface reconstruction is changed to ( $2 \times 2$ ) during growth, indicating the formation of  $\alpha$ -Sn. The schematic sample structure is shown in the inset of Fig. 1(a).

The  $\alpha$ -Sn samples are cleaved to about  $5 \times 5$  mm<sup>2</sup> squares for electrical measurements. The electrical transport measurements are performed in a physical-property measurement system (PPMS, Quantum Design,  $T_{\min} = 2$  K and  $B_{\max} = 9$  T) with an excitation current of 100  $\mu$ A. Measurements at higher magnetic fields are performed in an integrated superconducting-magnet system (TeslatronPT, Oxford instrument,  $T_{\min} = 1.5$  K and  $B_{\max} = 14$  T). Indium or silver paste is used as the contacts in a four-probe configuration.

## III. RESULTS AND DISCUSSION

Structural characterizations of the  $\alpha$ -Sn films are summarized in Fig. 1. The epitaxial growth of  $\alpha$ -Sn on InSb substrate is confirmed by reciprocal space mapping (RSM), as shown in Fig. 1(a). The  $\alpha$ -Sn peak appears below the InSb peak with the same in-plane lattice constant. The out-of-plane lattice constant of the  $\alpha$ -Sn film is calculated to be 6.499 Å, corresponding to an in-plane compressive strain or a uniaxial tensile strain. Additional

small peaks appearing periodically along the fully strained line are the thickness fringes, indicating the smooth surface of the film and a sharp interface between film and substrate. Figure 1(b) is a photograph of a quarter ( $\frac{1}{4} \times 2''$ )  $\alpha$ -Sn sample. No macroscopic defects, such as  $\beta$  phase, can be seen on the whole sample. The capability of large-area epitaxy is the prerequisite for device fabrication and integration. The alpha phase of Sn and high-quality interface are also verified by Raman spectra and cross-section transmission electron microscopy (TEM) in Figs. 1(c) and 1(d), respectively. A Raman peak can be clearly seen around 197 cm<sup>-1</sup>, which is the fingerprint of the alpha phase [37]. In Fig. 1(d), the high-angle annular dark-field scanning TEM (HAADF STEM) and corresponding energy-dispersive spectroscopy (EDS) show the sharp interface between  $\alpha$ -Sn and InSb, as well as the uniform thickness and chemical composition of the  $\alpha$ -Sn films. Figure 1(e) shows the surface morphology of the  $\alpha$ -Sn film revealed by atomic force microscopy (AFM). We can see striplike features on the surface that result from coherent growth on the InSb substrate (see Fig. S2 within the Supplemental Material [36]). Even with these features, the  $\alpha$ -Sn surface is quite smooth. For example, the surface roughness is only about 2 nm for a 100-nm-thick  $\alpha$ -Sn film. More structural characterizations, such as x-ray diffraction, on samples with different  $\alpha$ -Sn thicknesses can be found in previous work [38].

Figure 2 mainly shows the magnetotransport properties of the  $\alpha$ -Sn sample at low temperatures. The temperature-dependent resistance,  $R_{xx}$ , at different magnetic fields ( $B$ ) is shown in Fig. 2(a).  $R_{xx}$  is enhanced significantly under external  $B$  over the whole temperature range (2–300 K). Metallic behavior ( $dR_{xx}/dT > 0$ ) appears below 200 K, and at higher temperatures, it shows semiconducting behavior ( $dR_{xx}/dT < 0$ ). Figure 2(b) shows the MR at 2 K for the  $\alpha$ -Sn samples with different film thicknesses and InSb for comparison. The value of MR can be calculated by  $\Delta R_{xx}(B)/R_{xx}(0) \times 100\%$ . MR increases as the magnetic field increases up to 9 T with no sign of saturation. Notably, the MR value of the  $\alpha$ -Sn samples (over  $2.0 \times 10^4\%$  at 9 T) is about an order of magnitude larger than that of InSb (approximately  $2.0 \times 10^3\%$  at 9 T). Remarkably, clearer SdH oscillations can be seen on the MR curves of the  $\alpha$ -Sn samples, and the peaks appear at different fields from those of the InSb substrate, as indicated by the arrows in Fig. 2(b). Comparing Figs. 2(a) and 2(b), we believe the large MR is attributed to the  $\alpha$ -Sn films, rather than the InSb substrate. Since there is no essential difference among the  $\alpha$ -Sn samples with different thicknesses [see Fig. 2(b)], we mainly report the results on a 20-nm  $\alpha$ -Sn sample hereafter.

To show the topologically nontrivial character of the Dirac fermions in  $\alpha$ -Sn, the Berry phase is extracted from the SdH oscillations in the magnetoconductivity [39]. The measured resistivity can be converted into the

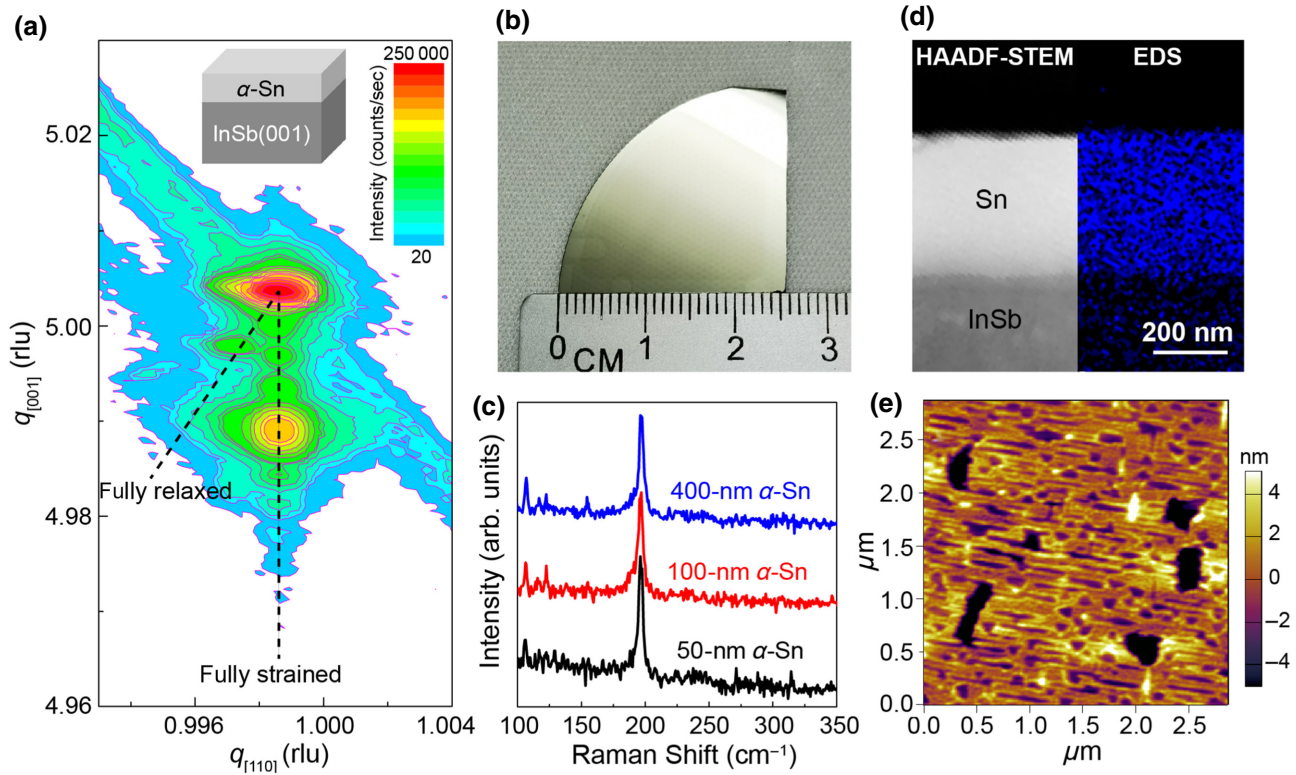


FIG. 1. Structural characterizations of  $\alpha$ -Sn samples. (a) RSM of the (115) plane of an  $\alpha$ -Sn sample. Dashed lines indicate fully strained and fully relaxed states.  $q[110]$  and  $q[001]$  are coordinates in reciprocal space and represent the in-plane and out-of-plane directions, respectively; rlu represents reciprocal lattice unit. Inset shows the sample structure. (b) Photograph of an as-grown  $\frac{1}{4} \times 2''$   $\alpha$ -Sn sample. (c) Raman spectra of  $\alpha$ -Sn samples with different thicknesses. Raman shift peak of  $\alpha$ -Sn is around  $197\text{ cm}^{-1}$ . (d) Cross-section HAADF STEM (left) and corresponding EDS (right) images of an  $\alpha$ -Sn sample. Sn signals are colored in blue. (e)  $\alpha$ -Sn surface morphology measured by AFM.

conductivity using

$$\sigma_{xx} = \frac{\rho_{xx}}{\rho_{yx}^2 + \rho_{xx}^2}, \quad \sigma_{xy} = \frac{\rho_{yx}}{\rho_{yx}^2 + \rho_{xx}^2}, \quad (1)$$

where  $\rho_{xx}$  and  $\rho_{yx}$  are the longitudinal resistivity and Hall resistivity, respectively. The longitudinal conductivity oscillations after subtracting the background are shown in Figs. 2(c) and 2(d), which can be described by the Lifshitz-Kosevich formula [40]:

$$\Delta\sigma_{xx} \propto \cos 2\pi \left( \frac{F}{B} - \gamma + \delta \right), \quad (2)$$

where the phase shift is  $\gamma = 1/2 - \phi_B/2\pi$  with Berry phase  $\phi_B$ .  $\delta$  is related to the Fermi-surface dimension, which is zero for a two-dimensional system and  $\pm 1/8$  for a 3D system, and  $F$  is the oscillation frequency. Therefore, the Berry phase can be extracted by plotting the Landau index versus magnetic field and fitting with

$$\frac{F}{B_N} = N + \gamma - \delta, \quad (3)$$

where  $B_N$  is the magnetic field at oscillation extrema. The oscillation maxima appear at the fields where the

Fermi level coincides with the  $N$ th Landau level. Therefore, we assign the maximum to integer  $N$  and minimum to half-integer  $N$ , and the extracted Berry phases are  $(-0.64 \pm 0.26)\pi$  for the  $\alpha$ -Sn sample and  $(0.06 \pm 0.14)\pi$  for InSb, as shown in Fig. 2(e). It is naturally expected because InSb is topologically trivial. Considering the phase shift,  $\delta$ , for the 3D Fermi surface, this change in Berry phase evidently shows the topologically nontrivial character of  $\alpha$ -Sn. We also confirm the conclusion from the analysis using the Hall conductivity oscillations (see Fig. S3 within the Supplemental Material [36]).

The fermiology of the  $\alpha$ -Sn films is further characterized by tilting-angle and temperature-dependent SdH oscillations. The shape and size of the Fermi surface can be demonstrated by the angle-dependent measurements, and the results are shown in Fig. 3(a). The experimental setup is shown in the inset of Fig. 3(a). The sample is rotated, so that the magnetic field is tilted at an angle,  $\theta$ , from the sample-surface normal ([001] direction) to the current direction ([110] direction). The MR magnitude is suppressed under the tilted  $B$ , and the shape of the Fermi surface can be estimated from the angle dependence of the oscillations. It can be seen that the oscillations are

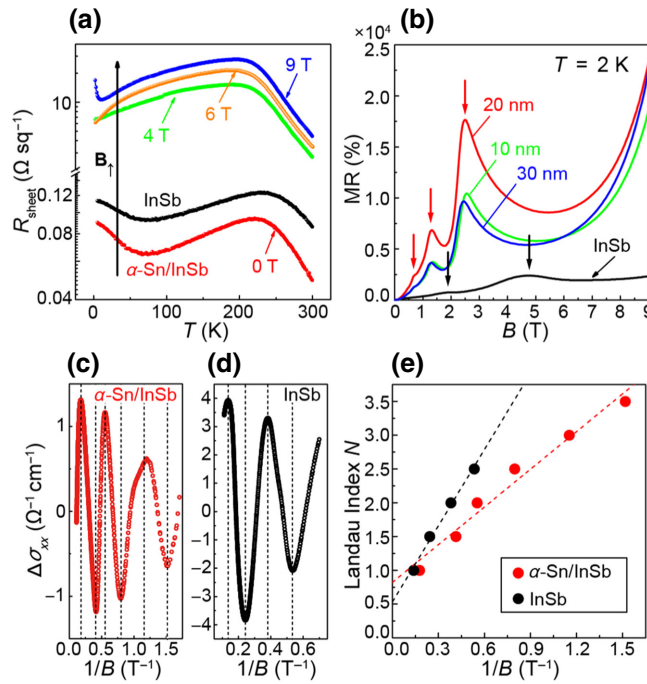


FIG. 2. Topologically nontrivial transport in  $\alpha$ -Sn samples. (a) Temperature-dependent resistance measured at 0, 4, 6, and 9 T on a 20-nm  $\alpha$ -Sn sample. (b) MR curves of  $\alpha$ -Sn samples with different thicknesses at 2 K. InSb data are shown for comparison. Arrows denote oscillation peaks. (c),(d) Longitudinal conductivity oscillations of the  $\alpha$ -Sn sample and InSb, respectively. (e) Landau index plots according to conductivity oscillations of the  $\alpha$ -Sn sample and InSb. Dashed lines are linear fittings using Eq. (3).

angle independent, which is indicative of a 3D spherical Fermi surface, while the oscillations from InSb (see Fig. S4 within the Supplemental Material [36]) have a slight shift, which may be due to the warped Fermi surface [41]. The spherical Fermi surface is expected for a diamond-structured Dirac semimetal with the Fermi level close enough to the Dirac point. Considering 20-nm  $\alpha$ -Sn as a bulk system and combining this with the previous predictions [22] and ARPES results [26,42], we believe our transport results can provide evidence for the 3D Dirac semimetal phase in  $\alpha$ -Sn. This is consistent with theoretical predictions that compressive strains can give rise to the Dirac semimetal phase in  $\alpha$ -Sn. We note that  $\alpha$ -Sn on InSb (001) is considered to be a topological insulator for thinner films ( $\leq 6.55$  nm) in several experimental studies [24,25,29], while our study shows that it is a Dirac semimetal with larger thicknesses ( $\geq 10$  nm). This suggests that a topological phase transition may occur between 6.55 and 10 nm for  $\alpha$ -Sn on InSb (001), which can be explained by the quantum-confinement effect, as discussed by de Coster *et al.* [43]. They point out that the quantum-confinement effect can open a bulk gap and induce a topologically insulating state in  $\alpha$ -Sn. As

the quantum-confinement effect becomes stronger with decreasing thickness, a topological phase transition from a Dirac semimetal to a topological insulator can occur in the  $\alpha$ -Sn films, even those that are compressively strained. It is reasonable that the thickness at which this phase transition occurs is much thinner on InSb than that on CdTe (approximately 40 nm [43]) because InSb provides a weaker quantum-confinement effect to  $\alpha$ -Sn.

Figure 3(b) shows the MR curves measured at selected temperatures. One can see that the SdH oscillations become weaker as the temperature increases and vanish above 30 K due to the thermal broadening of the Landau levels, as shown in the inset of Fig. 3(c). The decreased oscillation amplitude with temperature can be used to extract the effective mass using [18]

$$\Delta R_{xx}(B) \propto \frac{2\pi^2 k_B T m^*/\hbar e B}{\sinh(2\pi^2 k_B T m^*/\hbar e B)} , \quad (4)$$

where  $m^*$  is the carrier's effective mass,  $\hbar$  is the reduced Planck constant, and  $k_B$  is the Boltzmann constant. The magnetic field,  $B$ , is chosen to be 2.5 T for the  $\alpha$ -Sn sample. Fitting of the oscillation amplitudes from 2 to 30 K results in an effective mass of  $(0.039 \pm 0.001)m_0$  for the  $\alpha$ -Sn sample, where  $m_0$  is the rest mass of an electron. This value is slightly larger than the previously reported value ( $0.023m_0$ ) [44] for the  $\Gamma$  valley of  $\alpha$ -Sn but is still within the experimental uncertainty. This small effective mass is consistent with a Dirac band and usually leads to high mobility.

Careful observation of Fig. 3(b) shows two important properties: (1) an extremely large MR of over  $4.5 \times 10^5\%$  at 1.5 K and 14 T; and (2) a relatively large MR ( $> 3.0 \times 10^4\%$  at 9 T) persists within a wide temperature range (100–200 K) above the liquid-nitrogen point. The latter can be seen in Fig. 3(d), where MR at 9 T as a function of temperature is illustrated. The MR value of the  $\alpha$ -Sn sample increases until 100 K, then reaches a plateau ( $\text{MR} \sim 3.2 \times 10^4\%$ ) between 100 and 200 K, and finally decreases as the temperature increases to 300 K, consistent with the trend in Fig. 2(a). This unusual dependence is different from typical behavior, where MR decreases monotonically with temperature [5,45]. This indicates that a large MR is a robust property of the  $\alpha$ -Sn samples. This large MR is promising for highly sensitive magnetic sensing or storage. In particular, a magnetic sensitivity of about 13.4%/Oe can be estimated from the slope of the MR curve above 10 T at 1.5 K in the inset of Fig. 3(b), indicating it is possibly capable of being used for the detection and calibration of a small magnetic field on the order of 1 Oe.

The carrier concentration and mobility are calculated from the Hall resistance curves at selected temperatures in Fig. 3(e) using a single-band Drude model and the results are shown in Fig. 3(f). A lower carrier concentration ( $2.4 \times 10^{16} \text{ cm}^{-3}$  compared with  $1.3 \times 10^{17} \text{ cm}^{-3}$  of

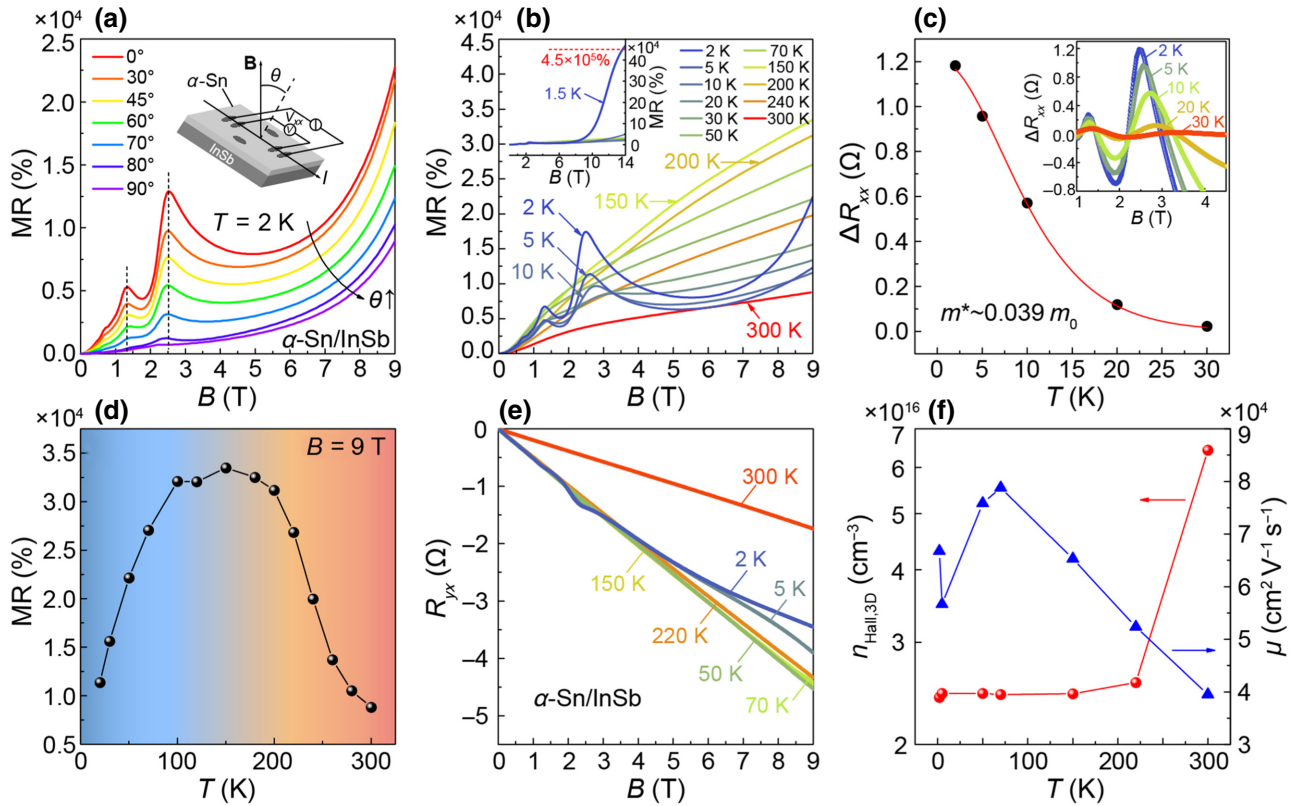


FIG. 3. Angle- and temperature-dependent magnetotransport properties of the  $\alpha$ -Sn sample. (a) Angle-dependent MR curves. Dashed lines are guides for the eye. Inset shows a schematic of the measurement configuration. (b) Temperature-dependent MR curves. Inset shows MR measured up to 14 T, yielding a value over  $4.5 \times 10^5\%$  at 1.5 K. (c) Oscillation amplitudes as a function of temperature. Red curve is the fitting curve using Eq. (4), resulting in an effective mass of  $m^* \sim 0.039 m_0$ . (d) MR at 9 T read from (b) as a function of temperature. (e) Temperature-dependent carrier concentration and mobility of the  $\alpha$ -Sn sample calculated from Hall effect measurements.

InSb at 2 K, as shown in Fig. S7 within the Supplemental Material [36]) ensures a higher mobility, on the order of  $5 \times 10^4 \text{ cm}^2 \text{ V}^{-1} \text{ s}^{-1}$ , in the  $\alpha$ -Sn samples. This carrier concentration is consistent with the value estimated from the frequency of the SdH oscillations. In a 3D system, the carrier concentration can be calculated by

$$n_{\text{SdH}} = \frac{1}{3\pi^2} \left( \frac{2eF}{\hbar} \right)^{3/2}, \quad (5)$$

with the frequency,  $F$ , obtained from the slopes of the fitting lines in Fig. 2(d), which is 1.86 T for the  $\alpha$ -Sn sample. The calculated  $n_{\text{SdH}}$  is  $1.4 \times 10^{16} \text{ cm}^{-3}$ , which is close to the value derived from the Hall measurement at 2 K. This consistency supports the 3D Fermi surface indicated by the SdH oscillations.

In this paragraph, we would like to discuss the MR in  $\alpha$ -Sn further. So far, a unified theory to explain the large MR in topological materials is missing and many physical origins have been proposed [5–7,46]. Here we attribute the large MR at 1.5 K and 14 T to the behavior of Dirac fermions in the extreme quantum limit. First, we estimate the Fermi energy from the carrier concentration.

The Fermi vector can be calculated by  $k_F = (3\pi^2 n_{\text{Hall}})^{1/3}$  to be about  $8.9 \times 10^{-3} \text{ Å}^{-1}$  and the corresponding Fermi energy,  $E_F = \hbar k_F v_F$ , is about 29 meV, assuming a Fermi velocity of  $5 \times 10^5 \text{ m/s}$ , as measured by ARPES [42]. This low Fermi energy is absolutely within the linear range of the Dirac bands and leads to a spherical Fermi surface. Second, we observe that the MR in our study is almost linear at higher magnetic fields ( $> 9$  T), as shown in the inset of Fig. 3(b), with no sign of saturation. Therefore, it is likely to result from the extreme quantum limit, where all the electrons occupy the lowest Landau level, according to the Abrikosov's model [47]. The condition to reach this state can be estimated by the criterion  $E_F < \hbar\omega_c$ , where  $\omega_c = eB/m^*$  is the cyclotron frequency. So, the magnetic field needed to realize the extreme quantum limit is about 5.75 T, which is well consistent with the experimental value of 5.81 T for the  $N = 1$  Landau index, as shown in Fig. 2(c). Finally, the large MR value at higher temperatures in Fig. 3(d) is probably due to high mobility, as the unusual MR versus  $T$  curve in Fig. 3(d) is similar to the temperature dependence of mobility in Fig. 3(e). In addition, this high mobility suggests a long transport-relaxation

time, which can be calculated from  $\mu = e\tau_{tr}/m^*$  to be about 870 fs. It is an order of magnitude larger than the value reported for  $\alpha$ -Sn capped with  $\text{AlO}_x$  [29]. A similar value has been obtained in a recent study [48]. This long relaxation time ensures that more nonequilibrium carriers can be transformed into charge or spin current. Therefore, further improvements of spin-charge conversion efficiency can be expected.

Finally, we perform a brief discussion with respect to the  $\alpha$ -Sn contribution in our samples. This can be demonstrated with a simple parallel-resistor model, as discussed in Sec. S8 within the Supplemental Material [36]. From this model, we can estimate a lower-limit contribution of  $\alpha$ -Sn of about 58% at 2 K, which is enough to show the nontrivial properties of  $\alpha$ -Sn films. This is consistent with the obvious difference between the  $\alpha$ -Sn samples and InSb substrate shown in Figs. 2 and 3.

#### IV. CONCLUSIONS

We successfully grow high-quality epitaxial  $\alpha$ -Sn films on the wafer scale on InSb substrates by MBE and show the topologically nontrivial character in these  $\alpha$ -Sn films through a transport study. Direct-transport evidence of a 3D Dirac semimetal phase and large magnetoresistance effects in  $\alpha$ -Sn are reported. A Berry phase of  $-0.64\pi$  and a 3D spherical Fermi surface support biaxially compressed  $\alpha$ -Sn being a Dirac semimetal, as theoretically predicted and observed by ARPES. In addition, a large MR of over  $4.5 \times 10^5\%$  at 1.5 K and over  $3.0 \times 10^4\%$  over a wide temperature range (100–200 K) is observed, which is probably due to the extreme quantum limit and high mobility, respectively. This Dirac semimetal  $\alpha$ -Sn on the wafer scale may be an ideal platform for the exploration of electronic and spintronic device applications. In particular, it is capable of highly sensitive magnetic sensing on the order of 1 Oe and promising for spintronic devices with higher spin-charge conversion efficiencies due to its longer transport-relaxation time (approximately 870 fs).

#### ACKNOWLEDGMENTS

The authors would like to acknowledge financial support from the National Key R&D Program of China (Grants No. 2018YFA0306200 and No. 2017YFA0303702) and the National Natural Science Foundation of China (NSFC) (Grants No. 51732006, No. 11890702, No. 51721001, No. 91750101, No. 21733001, No. 51861145201, No. 11874210, No. 51872134, and No. 11874210). Y. Ding and H.L. acknowledge support in characterization from Professor D. Wu and Professor X. Wu, and the helpful discussions with Professor H. Zhang and Professor M. Lu.

- [1] M. Z. Hasan and C. L. Kane, Colloquium: Topological insulators, *Rev. Mod. Phys.* **82**, 3045 (2010).
- [2] X.-L. Qi and S.-C. Zhang, Topological insulators and superconductors, *Rev. Mod. Phys.* **83**, 1057 (2011).
- [3] N. P. Armitage, E. J. Mele, and A. Vishwanath, Weyl and dirac semimetals in three-dimensional solids, *Rev. Mod. Phys.* **90**, 015001 (2018).
- [4] X. Wang, Y. Du, S. Dou, and C. Zhang, Room Temperature Giant and Linear Magnetoresistance in Topological Insulator  $\text{Bi}_2\text{Te}_3$  Nanosheets, *Phys. Rev. Lett.* **108**, 266806 (2012).
- [5] M. N. Ali, J. Xiong, S. Flynn, J. Tao, Q. D. Gibson, L. M. Schoop, T. Liang, N. Haldolaarachchige, M. Hirschberger, N. P. Ong, and R. J. Cava, Large, non-saturating magnetoresistance in  $\text{WTe}_2$ , *Nature* **514**, 205 (2014).
- [6] C. Shekhar, A. K. Nayak, Y. Sun, M. Schmidt, M. Nicklas, I. Leermakers, U. Zeitler, Y. Skourski, J. Wosnitza, Z. Liu, Y. Chen, W. Schnelle, H. Borrman, Y. Grin, C. Felser, and B. Yan, Extremely large magnetoresistance and ultrahigh mobility in the topological weyl semimetal candidate NbP, *Nat. Phys.* **11**, 645 (2015).
- [7] T. Liang, Q. Gibson, M. N. Ali, M. Liu, R. J. Cava, and N. P. Ong, Ultrahigh mobility and giant magnetoresistance in the dirac semimetal  $\text{Cd}_3\text{As}_2$ , *Nat. Mater.* **14**, 280 (2015).
- [8] N. Kumar, Y. Sun, N. Xu, K. Manna, M. Yao, V. Suss, I. Leermakers, O. Young, T. Forster, M. Schmidt, H. Borrman, B. Yan, U. Zeitler, M. Shi, C. Felser, and C. Shekhar, Extremely high magnetoresistance and conductivity in the type-II weyl semimetals  $\text{WP}_2$  and  $\text{MoP}_2$ , *Nat. Commun.* **8**, 1642 (2017).
- [9] J. Xiong, S. K. Kushwaha, T. Liang, J. W. Krizan, M. Hirschberger, W. Wang, R. J. Cava, and N. P. Ong, Evidence for the chiral anomaly in the dirac semimetal  $\text{Na}_3\text{Bi}$ , *Science* **350**, 413 (2015).
- [10] A. A. Burkov, Giant planar Hall effect in topological metals, *Phys. Rev. B* **96**, 041110(R) (2017).
- [11] S. Nandy, G. Sharma, A. Taraphder, and S. Tewari, Chiral Anomaly as the Origin of the Planar Hall Effect in Weyl Semimetals, *Phys. Rev. Lett.* **119**, 176804 (2017).
- [12] H. Li, H.-W. Wang, H. He, J. Wang, and S.-Q. Shen, Giant anisotropic magnetoresistance and planar Hall effect in the dirac semimetal  $\text{Cd}_3\text{As}_2$ , *Phys. Rev. B* **97**, 201110(R) (2018).
- [13] P. Li, C. Zhang, Y. Wen, L. Cheng, G. Nichols, D. G. Cory, G.-X. Miao, and X.-X. Zhang, Anisotropic planar Hall effect in the type-II topological weyl semimetal  $\text{WTe}_2$ , *Phys. Rev. B* **100**, 205128 (2019).
- [14] A. A. Taskin, S. Sasaki, K. Segawa, and Y. Ando, Manifestation of Topological Protection in Transport Properties of Epitaxial  $\text{Bi}_2\text{Se}_3$  Thin Films, *Phys. Rev. Lett.* **109**, 066803 (2012).
- [15] Y.-Y. Lv, L. Cao, Q.-Q. Yuan, S.-S. Chen, Z.-Q. Shi, Q.-Y. Li, Y. B. Chen, S.-H. Yao, J. Zhou, H. Wang, H. Zhang, S.-C. Li, D. Liu, and Y.-F. Chen, Theoretical and experimental evidence for the intrinsic three-dimensional dirac state in  $\text{Cu}_2\text{HgSnSe}_4$ , *Phys. Rev. B* **100**, 195147 (2019).
- [16] P. He, S. S. L. Zhang, D. Zhu, Y. Liu, Y. Wang, J. Yu, G. Vignale, and H. Yang, Bilinear magnetoelectric resistance as a probe of three-dimensional spin texture in topological surface states, *Nat. Phys.* **14**, 495 (2018).

- [17] P. Li, W. Wu, Y. Wen, C. Zhang, J. Zhang, S. Zhang, Z. Yu, S. A. Yang, A. Manchon, and X. X. Zhang, Spin-momentum locking and spin-orbit torques in magnetic nano-heterojunctions composed of weyl semimetal WTe<sub>2</sub>, *Nat. Commun.* **9**, 3990 (2018).
- [18] H. Murakawa, M. S. Bahramy, M. Tokunaga, Y. Kohama, C. Bell, Y. Kaneko, N. Nagaosa, H. Y. Hwang, and Y. Tokura, Detection of berry's phase in a bulk rashba semiconductor, *Science* **342**, 1490 (2013).
- [19] R. F. C. Farrow, D. S. Robertson, G. M. Williams, A. G. Cullis, G. R. Jones, I. M. Young, and P. N. J. Dennis, The growth of metastable, heteroepitaxial films of  $\alpha$ -Sn by metal beam epitaxy, *J. Cryst. Growth* **54**, 507 (1981).
- [20] S. Groves and W. Paul, Band Structure of Gray Tin, *Phys. Rev. Lett.* **11**, 194 (1963).
- [21] L. Fu and C. L. Kane, Topological insulators with inversion symmetry, *Phys. Rev. B* **76**, 045302 (2007).
- [22] H. Huang and F. Liu, Tensile strained gray tin: Dirac semimetal for observing negative magnetoresistance with shubnikov-de haas oscillations, *Phys. Rev. B* **95**, 201101 (2017).
- [23] D. Zhang, H. Wang, J. Ruan, G. Yao, and H. Zhang, Engineering topological phases in the luttinger semimetal  $\alpha$ -Sn, *Phys. Rev. B* **97**, 195139 (2018).
- [24] A. Barfuss, L. Dudy, M. R. Scholz, H. Roth, P. Hopfner, C. Blumenstein, G. Landolt, J. H. Dil, N. C. Plumb, M. Radovic, A. Bostwick, E. Rotenberg, A. Fleszar, G. Bihlmayer, D. Wortmann, G. Li, W. Hanke, R. Claessen, and J. Schafer, Elemental Topological Insulator with Tunable Fermi Level: Strained  $\alpha$ -Sn on InSb(001), *Phys. Rev. Lett.* **111**, 157205 (2013).
- [25] Y. Ohtsubo, P. Le Fevre, F. Bertran, and A. Taleb-Ibrahimi, Dirac Cone with Helical Spin Polarization in Ultrathin  $\alpha$ -Sn(001) Films, *Phys. Rev. Lett.* **111**, 216401 (2013).
- [26] C. Z. Xu, Y. H. Chan, Y. Chen, P. Chen, X. Wang, C. Dejoie, M. H. Wong, J. A. Hlevyack, H. Ryu, H. Y. Kee, N. Tamura, M. Y. Chou, Z. Hussain, S. K. Mo, and T. C. Chiang, Elemental Topological Dirac Semimetal:  $\alpha$ -Sn on InSb(111), *Phys. Rev. Lett.* **118**, 146402 (2017).
- [27] M. R. Scholz, V. A. Rogalev, L. Dudy, F. Reis, F. Adler, J. Aulbach, L. J. Collins-McIntyre, L. B. Duffy, H. F. Yang, Y. L. Chen, T. Hesjedal, Z. K. Liu, M. Hoesch, S. Muff, J. H. Dil, J. Schäfer, and R. Claessen, Topological surface state of  $\alpha$ -Sn on InSb(001) as studied by photoemission, *Phys. Rev. B* **97**, 075101 (2018).
- [28] V. A. Rogalev, F. Reis, F. Adler, M. Bauernfeind, J. Erhardt, A. Kowalewski, M. R. Scholz, L. Dudy, L. B. Duffy, T. Hesjedal, M. Hoesch, G. Bihlmayer, J. Schäfer, and R. Claessen, Tailoring the topological surface state in ultrathin  $\alpha$ -Sn(111) films, *Phys. Rev. B* **100**, 245144 (2019).
- [29] Q. Barbedienne, J. Varignon, N. Reyren, A. Marty, C. Vergnaud, M. Jamet, C. Gomez-Carbonell, A. Lemaitre, P. Le Fèvre, F. Bertran, A. Taleb-Ibrahimi, H. Jaffrès, J.-M. George, and A. Fert, Angular-resolved photoemission electron spectroscopy and transport studies of the elemental topological insulator  $\alpha$ -Sn, *Phys. Rev. B* **98**, 195445 (2018).
- [30] O. Vail, P. Taylor, P. Folkes, B. Nichols, B. Haidet, K. Mukherjee, and G. J. de Coster, Growth and magnetotransport in thin-film  $\alpha$ -Sn on CdTe, *Phys. Status Solidi B* **257**, 1800513 (2019).
- [31] M. H. Liao, Y. Y. Zang, Z. Y. Guan, H. W. Li, Y. Gong, K. J. Zhu, X. P. Hu, D. Zhang, Y. Xu, Y. Y. Wang, K. He, X. C. Ma, S. C. Zhang, and Q. K. Xue, Superconductivity in few-layer stanene, *Nat. Phys.* **14**, 344 (2018).
- [32] X. Zheng, J.-F. Zhang, B. Tong, and R.-R. Du, Epitaxial growth and electronic properties of few-layer stanene on InSb(111), *2D Mater.* **7**, 011001 (2019).
- [33] J. Ding, C. Liu, Y. Zhang, V. Kalappattil, R. Yu, U. Erugu, J. Tang, H. Ding, H. Chen, and M. Wu, Large damping enhancement in dirac-semimetal-ferromagnetic-metal layered structures caused by topological surface states, *Adv. Funct. Mater.* **31**, 2008411 (2021).
- [34] J. Ding, C. Liu, V. Kalappattil, Y. Zhang, O. Mosendz, U. Erugu, R. Yu, J. Tian, A. DeMann, S. B. Field, X. Yang, H. Ding, J. Tang, B. Terris, A. Fert, H. Chen, and M. Wu, Switching of a magnet by spin-orbit torque from a topological dirac semimetal, *Adv. Mater.* **33**, 2005909 (2021).
- [35] J. C. Rojas-Sanchez, S. Oyarzun, Y. Fu, A. Marty, C. Vergnaud, S. Gambarelli, L. Vila, M. Jamet, Y. Ohtsubo, A. Taleb-Ibrahimi, P. Le Fevre, F. Bertran, N. Reyren, J. M. George, and A. Fert, Spin to Charge Conversion at Room Temperature by Spin Pumping into a New Type of Topological Insulator:  $\alpha$ -Sn Films, *Phys. Rev. Lett.* **116**, 096602 (2016).
- [36] See the Supplemental Material at <http://link.aps.org/supplemental/10.1103/PhysRevApplied.17.014015> for the RHEED patterns, SEM images, and Hall conductivity oscillations of the InSb substrate and  $\alpha$ -Sn; the angle-dependent MR of other samples and the InSb substrate; FFT analysis of the oscillations; the temperature-dependent MR and Hall resistance of the InSb substrate; discussions on the contribution of the  $\alpha$ -Sn film in transport; and the topological phase transition induced by quantum-confinement effects.
- [37] J. Menéndez and H. Höchst, Study of the phase transition in heteroepitaxially grown films of  $\alpha$ -Sn by Raman spectroscopy, *Thin Solid Films* **111**, 375 (1984).
- [38] H. Song, J. Yao, Y. Ding, Y. Gu, Y. Deng, M.-H. Lu, H. Lu, and Y.-F. Chen, Thermal stability enhancement in epitaxial alpha Tin films by strain engineering, *Adv. Eng. Mater.* **21**, 1900410 (2019).
- [39] Y. Ando, Topological insulator materials, *J. Phys. Soc. Jpn.* **82**, 102001 (2013).
- [40] D. Shoenberg, *Magnetic Oscillations in Metals* (Cambridge University Press, Cambridge, England, 1984).
- [41] D. G. Seiler, Warped Fermi surface of the conduction band in InSb, *Phys. Lett. A* **31**, 309 (1970).
- [42] I. Madarevic, U. Thupakula, G. Lippertz, N. Claessens, P.-C. Lin, H. Bana, S. Gonzalez, G. Di Santo, L. Petaccia, M. N. Nair, L. M. C. Pereira, C. Van Haesendonck, and M. J. Van Bael, Structural and electronic properties of the pure and stable elemental 3D topological dirac semimetal  $\alpha$ -Sn, *APL Mater.* **8**, 031114 (2020).
- [43] G. J. de Coster, P. A. Folkes, P. J. Taylor, and O. A. Vail, Effects of orientation and strain on the topological characteristics of CdTe/ $\alpha$ -Sn quantum wells, *Phys. Rev. B* **98**, 115153 (2018).
- [44] B. L. Booth and A. W. Ewald, Anisotropy of the gray-tin  $\Gamma_8^+$  conduction band, *Phys. Rev.* **168**, 805 (1968).

- [45] J. Feng, Y. Pang, D. Wu, Z. Wang, H. Weng, J. Li, X. Dai, Z. Fang, Y. Shi, and L. Lu, Large linear magnetoresistance in dirac semimetal Cd<sub>3</sub>As<sub>2</sub> with Fermi surfaces close to the dirac points, *Phys. Rev. B* **92**, 081306(R) (2015).
- [46] G. Zheng, X. Zhu, Y. Liu, J. Lu, W. Ning, H. Zhang, W. Gao, Y. Han, J. Yang, H. Du, K. Yang, Y. Zhang, and M. Tian, Field-induced topological phase transition from a three-dimensional weyl semimetal to a two-dimensional massive dirac metal in ZrTe<sub>5</sub>, *Phys. Rev. B* **96**, 121401(R) (2017).
- [47] A. A. Abrikosov, Quantum magnetoresistance, *Phys. Rev. B* **58**, 2788 (1998).
- [48] I. Madarevic, N. Claessens, A. Seliverstov, C. Van Haesendonck, and M. J. Van Bael, Non-trivial quantum magnetotransport oscillations in pure and robust topological  $\alpha$ -Sn films, [arXiv:2002.12248v2](https://arxiv.org/abs/2002.12248v2) (2020).